

Minor-merger induced star formation rejuvenation in an elliptical radio-loud quasar host, 3C 59

YIJUN WANG,^{1,2} TAO WANG,^{1,2} KE XU,^{1,2} JUNJIE MAO,³ YERONG XU,^{4,5} AND ZHENG ZHOU⁶

¹*School of Astronomy and Space Science, Nanjing University, 163 Xianlin Avenue, Nanjing 210023, People's Republic of China*

²*Key Laboratory of Modern Astronomy and Astrophysics, Nanjing University, Ministry of Education, 163 Xianlin Avenue, Nanjing 210023, People's Republic of China*

³*Department of Astronomy, Tsinghua University, Haidian DS 100084 Beijing, People's Republic of China*

⁴*Department of Astronomy & Physics, Saint Mary's University, 923 Robie Street, Halifax, NS B3H 3C3, Canada*

⁵*Istituto Nazionale di Astrofisica – Istituto di Astrofisica Spaziale e Fisica Cosmica di Palermo, Via U. La Malfa 153, I-90146 Palermo, Italy*

⁶*Department of Astronomy, Xiamen University, Xiamen, Fujian 361005, People's Republic of China*

ABSTRACT

We report a rare case where an elliptical radio-loud quasar host, 3C 59, rejuvenates star formation activity through minor mergers with its nearby satellite galaxies. The inferred star formation history of 3C 59 shows significant star formation rejuvenation within the past 500 Myr, before which remains rather quiescent for most of the cosmic time. Three nearest satellite galaxies of 3C 59 exhibit significant morphological disturbances, and two of them present strong tidal tails pointing towards 3C 59. In addition, all the satellite galaxies within a projected distance of 200 kpc show low star formation activities. They also have systematically lower effective radius (R_e) than local late-type galaxies, while 3C 59 has significantly larger R_e than both early- and late-type galaxies. All these features suggest that ongoing minor mergers between 3C 59 and its nearby satellites could be causing gas to flow into 3C 59, which induces the star formation rejuvenation, and possibly also triggers the quasar activity. The enormous power from the large-scale radio jet of 3C 59 may in turn help keep the halo hot, prevent gas cooling, and further reduce star formation in its satellite galaxies. These results provide important insights into the mass and size growth of central galaxies and star formation quenching of satellite galaxies in galaxy groups.

Keywords: Galaxy groups (597) — Galaxy mergers (608) — Radio loud quasars (1349) — Radio lobes (1348) — Lenticular galaxies (915) — Elliptical galaxies (456)

1. INTRODUCTION

Galaxies are mainly divided into two different populations in the star-formation rate vs. stellar mass diagram: star-forming galaxies (SFGs) with evident star formation and quiescent galaxies (QGs) with little or no star formation (e.g., Noeske et al. 2007; Moustakas et al. 2013; Renzini & Peng 2015). A widely accepted evolutionary scenario is that SFGs stop or reduce star formation and further transform into QGs (e.g., Faber et al. 2007; Peng et al. 2010).

However, some QGs experience significant star formation bursts after a long period of low star formation,

so-called “rejuvenation” (e.g., Rowlands et al. 2018; Chauke et al. 2019), which improves our understanding on galaxy evolution. One rejuvenation event may form 10% of the total mass (Chauke et al. 2019; Tacchella et al. 2022). Galaxies, especially massive ones, may experience multiple rejuvenation events (Tanaka et al. 2024), so the contributions of rejuvenation processes to the growth of galaxies are expected to be non-negligible. Recently, Pandey et al. (2024) found that star formation exits in all early-type galaxies in the nearby Universe, which suggests that rejuvenation is a constant process. In addition, Mancini et al. (2019) argued that rejuvenations may be responsible for the bending of the star-forming main sequence at high-mass end.

Despite the importance of rejuvenation, the nature and mechanism of rejuvenation still remain unclear. Based on a simulation, Kaviraj et al. (2009) demon-

strate that gas accretion during gas-rich minor mergers can trigger rejuvenation processes in early-type galaxies. Other studies also suggest that these processes may further enable early-type galaxies turn into red spirals or S0 galaxies (e.g., Diaz et al. 2018; Hao et al. 2019; Rathore et al. 2022). However, there is still a lack of direct observational evidences for the connection between rejuvenation and mergers. Recently, Paudel et al. (2023) found an early-type dwarf galaxy is rejuvenating star formation through accreting gas from a nearby star-forming dwarf galaxy. In this work, we report another rare case where a radio-loud active galactic nuclei (AGN), 3C 59, hosted by an early-type galaxy is rejuvenating star formation activity through ongoing minor mergers with its nearby satellite galaxies.

This paper is organized as follows. Section 2 describes the identification of satellite galaxies for 3C 59. Section 3 introduces the observational data used to construct the broadband spectral energy distribution (SED). Section 4 describes the details about the image decomposition that obtains the structure properties of all the galaxies. Section 5 introduces the detailed SED fitting processes. We discuss the results in Section 6 and summarize them in Section 7. Throughout this paper, we assume a flat cosmology with the following parameters: $\Omega_m = 0.3$, $\Omega_\Lambda = 0.7$, and $H_0 = 70 \text{ km s}^{-1} \text{ Mpc}^{-1}$.

2. IDENTIFY SATELLITE GALAXIES FOR 3C 59

3C 59 is a Fanaroff-Riley Class II (FR II) radio AGN with a large-scale radio jet extending to ~ 150 kpc (see Figure 1). It has a spectroscopic redshift of $z_{\text{spec},3\text{C}59} = 0.1096$ (Eracleous & Halpern 2004) and a photometric redshift of $z_{\text{phot},3\text{C}59} = 0.1424 \pm 0.0161$ in Sloan Digital Sky Survey (SDSS) survey (Ahumada et al. 2020). Satellite galaxies of 3C 59 were selected by the following criteria: (1) the projected distance to 3C 59 should be less than 200 kpc because 200 kpc may be a threshold for the virial radius of 3C 59 dark matter halo (see details in Section 6.2); (2) the redshift difference between each satellite and 3C 59 should be less than the redshift uncertainty of each satellite ($\delta_{z_{\text{phot},\text{sate}}}$): $|z_{\text{phot},\text{sate}} - z_{\text{spec},3\text{C}59}| \leq \delta_{z_{\text{phot},\text{sate}}}$ or $|z_{\text{phot},\text{sate}} - z_{\text{phot},3\text{C}59}| \leq \delta_{z_{\text{phot},\text{sate}}}$. Most of the galaxies that lie around 3C 59 in projection only have photometric redshifts from SDSS survey. Their photometric redshifts are estimated through the kd-tree nearest neighbor fit based on SDSS data at u , g , r , i , and z filters (Beck et al. 2016). This fit method is adopted via a spectroscopic training set comprised of 1 976 978 galaxies, which are relatively accurate with a standard deviation of 0.0205 (Beck et al. 2016). Finally, we found five satellite galaxies and named them A, B, C, D, and

E in order of closest to farthest from 3C 59 (see the green circles in Figure 1). The projected distance from Satellites A, B, C, D, and E to 3C 59 is about 56 kpc, 62 kpc, 84 kpc, 126 kpc, and 145 kpc, respectively. Their photometric redshifts given by SDSS survey are 0.1262 ± 0.0245 for Satellite A, 0.1263 ± 0.0405 for Satellite B, 0.1344 ± 0.0179 for Satellite C, 0.1382 ± 0.0178 for Satellite D, and 0.0964 ± 0.0405 for Satellite E (also see Figure 1).

3. OBSERVATIONAL DATA

3.1. Optical and radio images

Optical images at g , r , and z filters (see the RGB image in Figure 1) were derived from the Dark Energy Spectroscopic Instrument (DESI) Legacy Imaging Surveys Data Release 9 (DR9). Depth of **imaging** decreases from g filter to z filter (Dey et al. 2019). The 5σ point source (AB) depths with single exposure¹ are ~ 24.2 mag for g filter, ~ 23.9 mag for r filter, and ~ 22.7 mag for z filter. Therefore, in the following analysis, we mainly used the results obtained with g -filter image that has the highest data quality due to the deepest imaging.

The 3 GHz radio image (see the red contour in Figure 1) was derived from the Very Large Array Sky Survey (VLASS; Lacy et al. 2020) Epoch 2.2.

3.2. Data used for constructing a broadband SED of 3C 59

To construct a broadband SED with the Code Investigating GALaxy Emission (CIGALE; Burgarella et al. 2005; Noll et al. 2009; Boquien et al. 2019; Yang et al. 2020, 2022) (see Section 5.1), we simultaneously utilized the multi-wavelength photometric data from the historical published catalogs and the optical spectrum from the Large Sky Area Multi-Object Fiber Spectroscopic Telescope (LAMOST).

Multi-wavelength photometric data: The multi-wavelength data from UV to radio bands were collected from the following multiple surveys: Galaxy Evolution Explorer (GALEX), SDSS, Two Micron All-Sky Survey (2MASS), Wide-field Infrared Survey Explorer (WISE), Infrared Astronomical Satellite (IRAS), VLASS, and very long baseline interferometry (VLBI). The cross-matching radius with each catalog is $1''$. We refer readers to Appendix A for detailed introduction about these surveys and data. In Table A1, we summarize the information about the multi-wavelength data.

LAMOST optical spectrum (3700–9000 Å): CIGALE cannot directly analyze spectrum data. Therefore, we

¹ See details in <https://www.legacysurvey.org/dr9/description/>

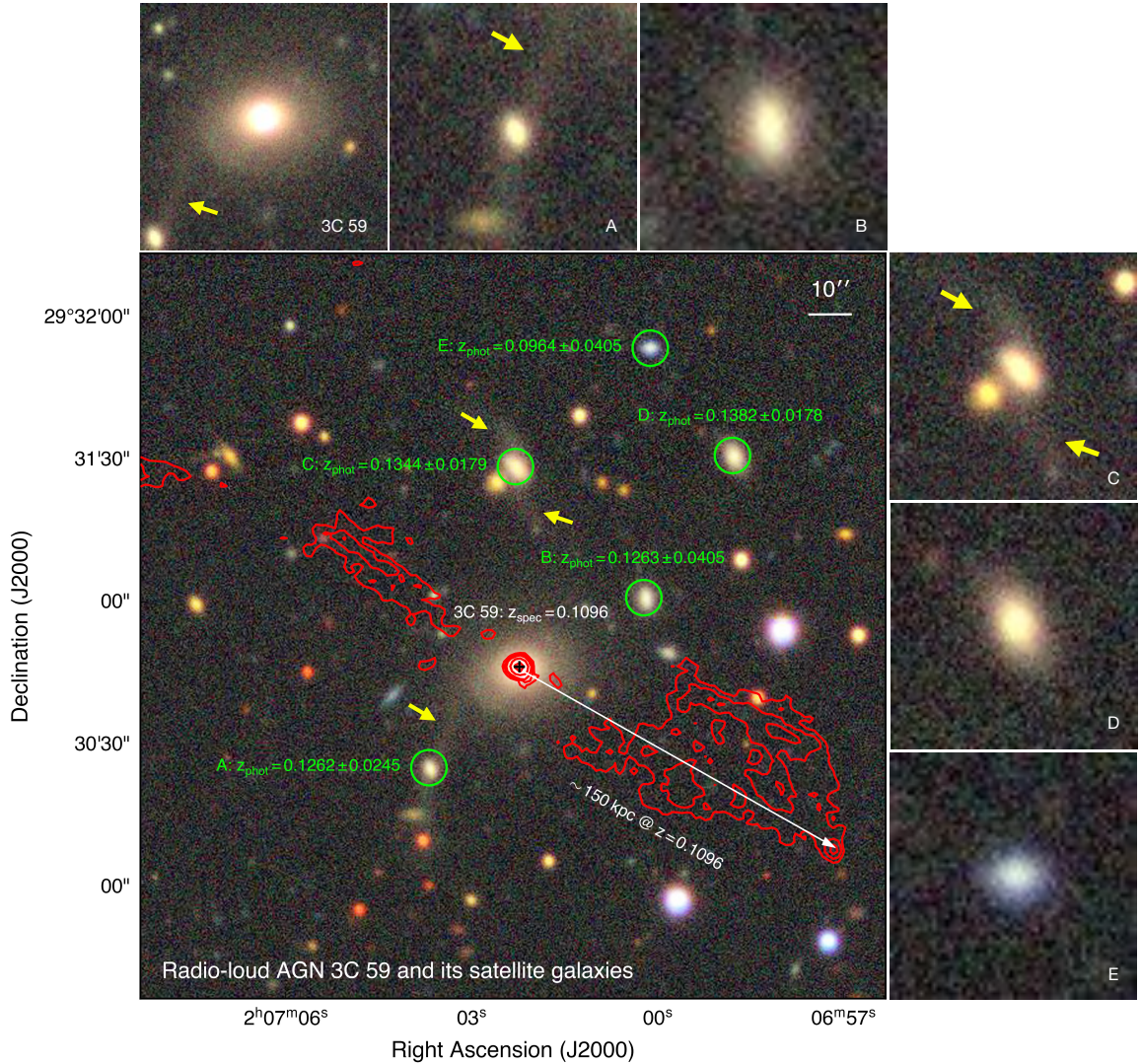


Figure 1. Images for 3C 59 (the black cross) and its five satellite galaxies (A, B, C, D, and E; the green circles). The background shows an RGB image of DESI g , r , and z filters. The red contour represents the VLASS 3 GHz data, and the contour levels are 5σ , 8σ , 12σ , 30σ , and 70σ ($\sigma \sim 0.18 \text{ mJy beam}^{-1}$). The white arrow represents the distance from 3C 59 to the edge of the radio lobe ($\sim 150 \text{ kpc}$ at $z = 0.1096$). The yellow arrows highlight the tidal tails. The six small panels show the individual galaxies zoomed in.

selected eight continuum ranges in the calibrated LAMOST spectrum (see the yellow regions in Figure B1), and the average wavelength and flux of each range were utilized in the SED fitting. We refer readers to Appendix B for more details about the LAMOST spectrum.

3.3. Data used for constructing broadband SEDs of the five satellite galaxies

For the five satellite galaxies, we collected historical public data from SDSS, WISE, and 2MASS surveys. The cross-matching radius with each catalog is $1''$. The basic informations about these data are summarized in Table A2.

For 3C 59 and all the satellite galaxies, we followed Schlafly & Finkbeiner (2011) to make the Galactic extinction correction for all the observational data including photometric data and the LAMOST spectrum. In this process, we adopted the Fitzpatrick (1999) reddening law with $R_V = 3.1$ based on the dust map from Schlegel et al. (1998).

4. TWO-DIMENSIONAL DESI IMAGE DECOMPOSITION

The image decomposition for DESI images at g , r , and z filters were performed based on GALIGHT software (Ding et al. 2021), which is a Python code that provides various processing tools and two-dimensional (2D) pro-

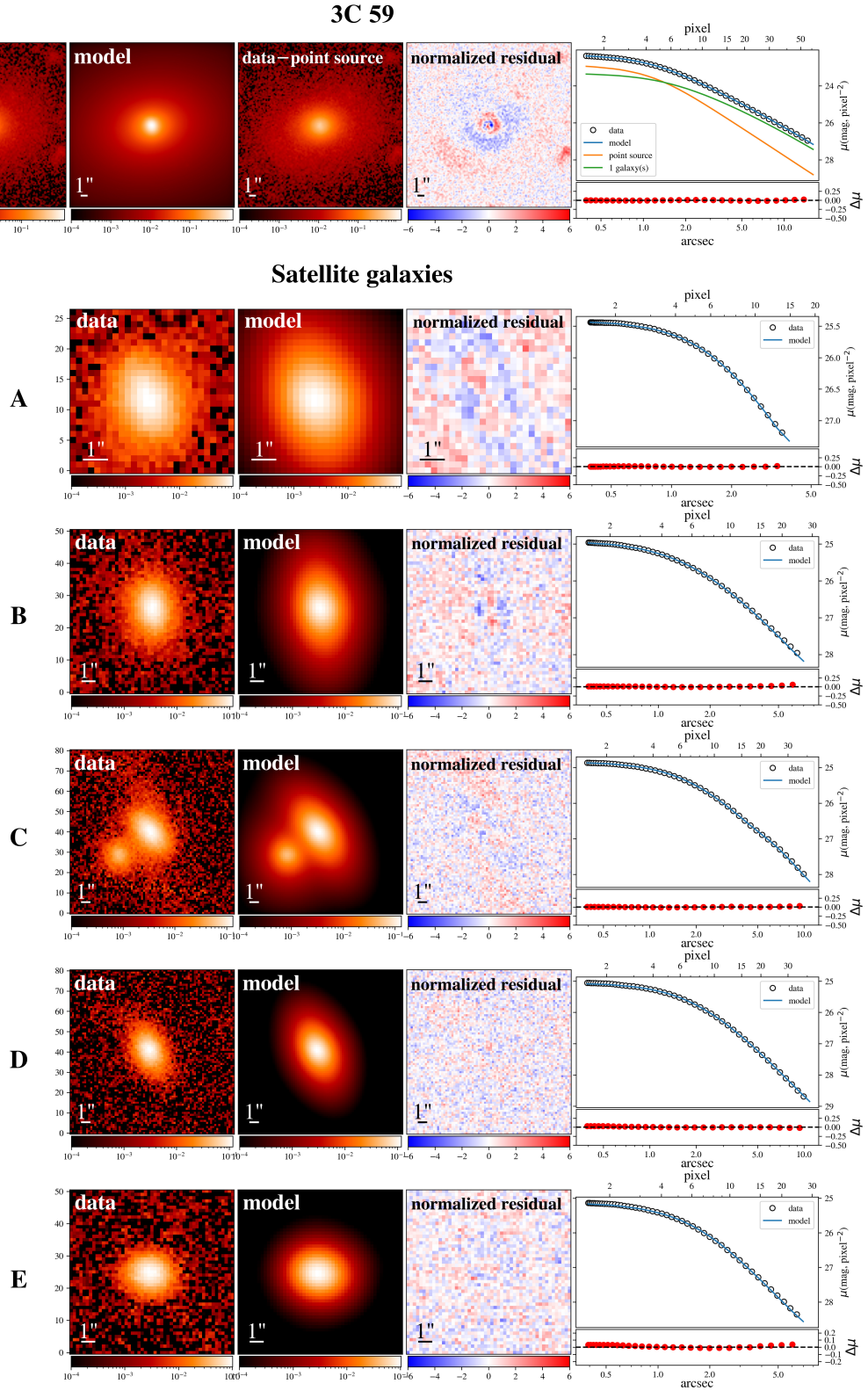


Figure 2. 2D decomposition of 3C 59 and the five satellite galaxies for the DESI g -band images with GALIGHT. The first row is shown for 3C 59, while the panels from left to right represent data, model, data minus point source (host galaxy only), normalized residual (data–model/noise), and surface brightness profile, respectively. The second row to the sixth row are shown for Satellites A, B, C, D, and E, respectively, while in each row, the panels from left to right represent data, model, normalized residual, and surface brightness profile, respectively.

file fitting for astronomical data. For 3C 59 and the five satellite galaxies, the best-fit parameters, such as the effective radius (R_e), Sérsic index ($n_{\text{sérsic}}$), AGN fluxes, and reduced χ^2 at each filter, are summarized in Table C1.

4.1. Image decomposition for 3C 59

The AGN component was modeled using an empirical point-spread function (PSF) based on stars within the DESI survey area, while the host galaxy component was modeled as a smooth Sérsic profile. The 2D decomposition at g filter is shown in Figure 2. The decompositions at r and z filters show similar results, so we do not exhibit them here. The AGN fluxes at g , r , and z filters were determined using a combined PSF model based on two stars within a $3' \times 3'$ area centered on 3C 59, which had the lowest reduced χ^2 for the fit. The uncertainties of the fluxes were estimated using five PSF models, each constructed from different stars. In addition, simultaneously freeing the parameters of the PSF and Sérsic profiles results in a degeneracy among parameters. Thus, we made the 2D profile fitting with two tests: (1) $n_{\text{sérsic}}$ is fixed to 4 that is a rough approximation of elliptical galaxies; (2) $n_{\text{sérsic}}$ is fixed to 1 that is an approximation of disk galaxies. The fitting with $n_{\text{sérsic}} = 4$ shows a better fit comparing to assuming $n_{\text{sérsic}} = 1$. Therefore, we conclude that the host galaxy of 3C 59 shows an elliptical morphology.

4.2. Image decomposition for satellite galaxies

Each satellite galaxy was well modeled with only one smooth Sérsic profile. The decomposition result for the g -filter image is shown in Figure 2. The decompositions for r - and z -filter images show similar results, which are not presented here. All the satellite galaxies show a low $n_{\text{sérsic}}$ (~ 1 or ~ 2), which indicates a disk (late-type) morphology. However, these galaxies do not show significant spiral structures, which are consistent with S0 galaxy type (see Figure 2).

5. BROADBAND SED ANALYSIS

We constructed the broadband SED with CIGALE. The CIGALE is a Python code that efficiently models the observational multi-wavelength data from X-ray to radio bands using a series of AGN/galaxies templates. Based on the Bayesian-like approach, this code estimates many fundamental physical properties of host galaxies and AGN, such as star formation rate (SFR), stellar mass (M_*), dust luminosity, AGN contribution and other quantities.

5.1. Broadband SED fitting for 3C 59

Simultaneously fitting AGN and host galaxy components of 3C 59 cannot better constrain the various parameters. Therefore, we firstly obtained the best-fit model for AGN and dust components, and then fixed them in the entire broadband SED fitting.

Fitting for the AGN and dust components: We used the AGN module (Stalevski et al. 2012, 2016), the dust emission (Dale et al. 2014), and the radio module in CIGALE to simultaneously fit the AGN fluxes at DESI g , r , and z filters (see details in Section 4.1), and photometric data from WISE, VLA, and VLBI. At the reference wavelength of these data, SED is dominated by AGN or correlated with dust emission. In addition, we did not consider the minor contribution of the nebular emission to the radio continuum. The model parameter settings in the fit are summarized in Table D1. The best-fit SED is shown in Figure D1, the best-fit model parameters are listed in Table D2, and the best-fit AGN properties are summarized in Table 1. We refer readers to Appendix E for detailed discussions about AGN properties of 3C 59.

Fitting for the entire broadband SED: In addition to AGN, dust, and radio modules whose model parameters were fixed to the best-fit values obtained above, we used three additional modules to fit all the multi-wavelength data of 3C 59. These three modules are the delayed τ star formation history (SFH), the Bruzual & Charlot (2003) simple stellar population model, and the Calzetti et al. (2000) galaxy dust attenuation. These modules and their parameter settings are summarized in Table D2, and the best-fit results for the host galaxy properties are listed in Table 1. The best-fit SED is shown in Panel (a) of Figure 3.

5.2. SED fitting for satellite galaxies

For each satellite galaxy, the galaxy templates include the following three modules: the delayed τ SFH, the Bruzual & Charlot (2003) simple stellar population model, and the Calzetti et al. (2000) galaxy dust attenuation. These modules and their parameter settings are summarized in Table D3. As we mentioned in Section 2, photometric redshifts of SDSS surveys are estimated based on solely SDSS data. In this work, we also included WISE (and 2MASS) data in addition to SDSS data. Therefore, to find a suitable redshift value applied in the SED fitting, we fixed the redshift value of each satellite galaxy to SDSS photometric redshift and spectroscopic redshift of 3C 59, respectively. We found that for Satellites A, B, and C, fixing to the spectroscopic redshift of 3C 59 provides a better fitting (lower reduced χ^2) than fixing to the SDSS photometric redshifts, while for Satellites D and E, the opposite is true.

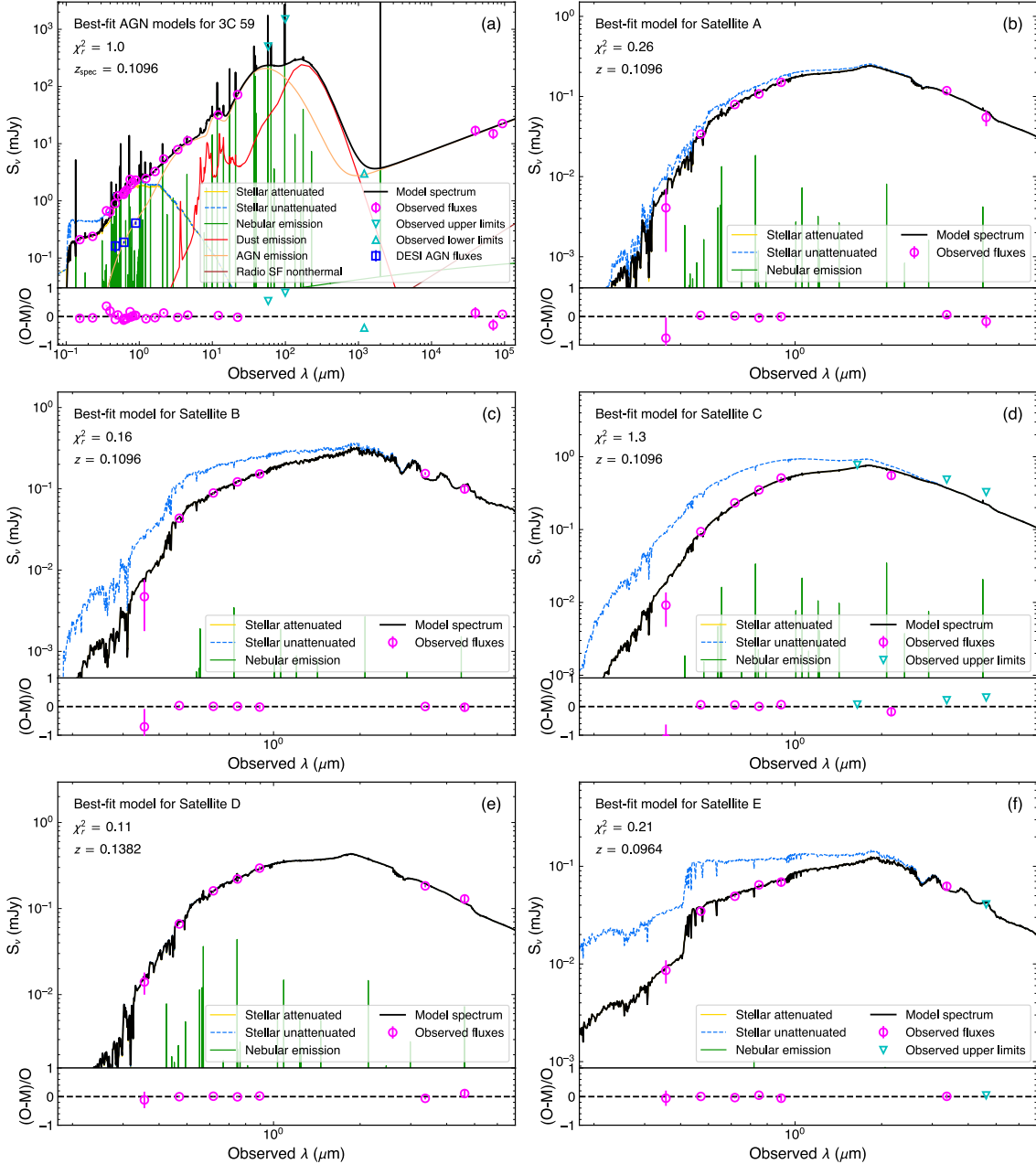


Figure 3. Best-fit broadband SED model with CIGALE for 3C 59 (Panel a) and the five satellite galaxies (Panels b–f). The details about the observational data used for SED fitting are introduced in Section 3, and shown in Tables A1 and A2. The details about DESI AGN fluxes are introduced in Section 4 and shown in Table C1.

Therefore, the redshift value applied in the SED fitting is 0.1096 for Satellite A/B/C, 0.1382 for Satellite D, and 0.0964 for Satellite E (see Table 1). The best-fit SEDs are shown in Figure 3.

6. RESULTS AND DISCUSSION

6.1. Star formation rejuvenation in 3C 59

We combined two methods to decide the star-formation properties of each galaxy: (1) the star-forming main sequence; (2) rest-frame UVJ color diagram. Throughout this work, we adopted the main sequence from Popesso et al. (2023) and UVJ selection criteria from Schreiber et al. (2015). The main sequence from Popesso et al. (2023) is obtained based on a Kroupa (2001) initial mass function (IMF), while we adopted a

Table 1. Best-fit physical and structure properties for 3C 59 and the five satellite galaxies (A, B, C, D, and E)

Component	Parameter	Symbol	3C 59	A	B	C	D	E
	Redshift used in the fitting	z_{CIGALE}	0.1096	0.1096	0.1096	0.1096	0.1382	0.0964
Host galaxy	Stellar mass	M_{\star} ($10^{10} M_{\odot}$)	4.37 ± 0.92	0.80 ± 0.27	0.57 ± 0.27	3.02 ± 1.03	2.29 ± 0.78	0.10 ± 0.04
	Star formation rate	SFR ($M_{\odot} \text{ yr}^{-1}$)	6.21 ± 0.71	< 0.21	< 1.09	< 0.39	< 0.32	< 2.39
	Dust attenuation	E(B-V) (mag)	0.077 ± 0.004	0.14 ± 0.12	0.28 ± 0.16	0.25 ± 0.17	0.10 ± 0.10	0.26 ± 0.13
	8–1000 μm dust luminosity	$L_{\text{IR,dust}}$ (10^{37} W)	2.42 ± 0.12
AGN	AGN dust reemitted luminosity	$L_{\text{IR,AGN}}$ (10^{37} W)	9.81 ± 0.66
	Fraction of $L_{\text{IR,AGN}}$ to $L_{\text{IR,tot}}$	F_{AGN}	0.80 ± 0.11
	Polar dust attenuation	E(B-V) (mag)	0.83 ± 0.07
	AGN radio-loudness	R_{AGN}	14 ± 2
	Radio spectral index of AGN	α_{AGN}	0.41 ± 0.12
	Viewing angle	θ_{AGN} ($^{\circ}$)	23 ± 14

Chabrier (2003) IMF in the SED fitting with CIGALE. Therefore, we multiplied M_{\star} and SFR of the main sequence in Popesso et al. (2023) by a factor of 1.06 (Speagle et al. 2014) to convert values from the Kroupa (2001) IMF to the Chabrier (2003) IMF. 3C 59 is located above the main sequence (see Panel c of Figure 4), and resides in the star-forming region in the UVJ diagram (see Panel d of Figure 4). Combining these two methods, we classified the host galaxy of 3C 59 as an SFG.

The reduced χ^2 of 2D image decomposition (see Table C1) decreases from Satellite A to E (distance to 3C 59 from small to large, see Panel a of Figure 4), which indicates that the closer the satellite galaxies are to 3C 59, the more significant the morphological disturbances are. In addition, Satellites A and C exhibit significant tidal tails pointing towards 3C 59 (highlighted by yellow arrows in Figure 1 and gray lines in Panel a of Figure 4). The effective radius of 3C 59 is much larger than the scaling relations for local early- and late-type galaxies (Lange et al. 2015) (see Panel b of Figure 4). This result indicates that 3C 59 is undergoing a dramatic size growth, while many works have demonstrated that minor merger may be the main driver of size growth in early-type galaxies (e.g., Naab et al. 2009; López-Sanjuan et al. 2012; Bédorf & Portegies Zwart 2013; Kaviraj et al. 2014; Oogi et al. 2016; Matharu et al. 2019). These pieces of observational evidences suggest that 3C 59 is undergoing a minor merger with its nearby satellite galaxies.

To investigate whether the minor merger affects star formation activities in 3C 59, we simultaneously fitted the multi-wavelength photometric data and LAMOST spectrum of 3C 59 with PROSPECTOR (Leja et al. 2017; Johnson et al. 2021). The PROSPECTOR is a robust code that can provide a non-parametric SFH. In the fit, we removed strong emission lines and subtracted AGN continuum model (obtained with CIGALE) from the observational data to exclude the bias brought by AGN activ-

ities. We refer readers to Appendix F for more details about the parameter setting in the fit. The SFH of 3C 59 shows a significant rejuvenation of star formation activities within the past 500 Myr, before which remains rather quiescent for most of the cosmic time (see Figure 5). For the five satellite galaxies, we cannot well constrain their SFHs due to the lack of sufficient multi-wavelength data.

The ongoing minor mergers and star formation rejuvenation in 3C 59 indicate that 3C 59 may be accreting cold gases from satellites to rejuvenate star formation activity and increase size. Minor mergers may also trigger quasar activities and promote central black holes growth through enhanced gas supply (Wang et al. 2023).

6.2. How the physical properties of 3C 59 affect star formation activities of satellite galaxies

Due to the data limitation, we only obtained the upper limits of SFR for all the satellite galaxies, most of which are below the main sequence (see Panel c of Figure 4). In the UVJ color diagram, all the five satellite galaxies are located at the quiescent region (see Panel d of Figure 4). Thus, we classified all the five satellite galaxies as QGs. Next we discuss some possible mechanisms to explain the star formation quenching in these satellite galaxies.

- (1) *Galaxy interaction strips gas in satellite galaxies.* The interaction between 3C 59 and satellite galaxies may result in a gas loss in satellite galaxies, and further reduce their star formation activities. Satellites A, B, and C show ongoing interaction features with 3C 59 but have reduced star formation much earlier (old stellar population; see Panel d of Figure 4). It implies that their star formation quenching occurs earlier than the ongoing galaxy interaction. As for Satellites D and E, the two farthest satellites, they do not show significant interaction features. Their young stellar populations (see Panel d of Figure 4), indicators

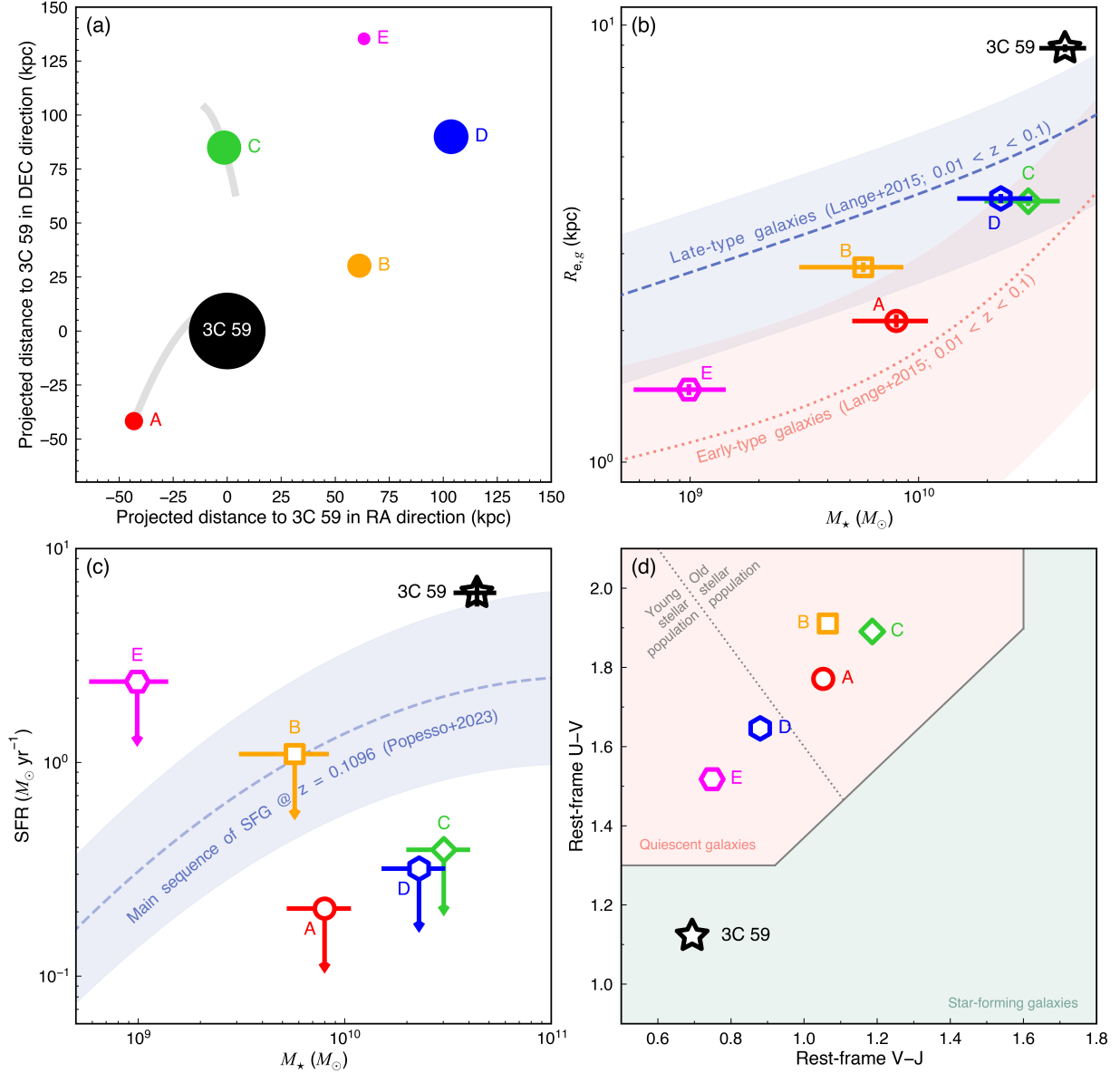


Figure 4. Structure properties and star formation properties of 3C 59 and the five satellite galaxies (A, B, C, D, and E). *Panel (a)*: Projected distance of each satellite galaxy to 3C 59. The radius of each circle is equal to $2R_{e,g}$ where $R_{e,g}$ is the DESI g -filter effective radius (see Section 4 and Table C1). The gray solid lines represent cartoon drawings of the tidal tails that correspond to the structures highlighted by the yellow arrows in Figure 1. *Panel (b)*: M_* - $R_{e,g}$ relation. The M_* is the stellar mass (see Section 5 and Table 1). The blue and red regions show the M_* - R_e relations for local late- and early-type galaxies (Lange et al. 2015), respectively. *Panel (c)*: M_* -SFR relation. SFR is the star formation rate (see Section 5 and Table 1). *Panel (d)*: Rest-frame UVJ diagram. Rest-frame U, V, and J magnitudes are estimated from the best-fit broadband SED (see Fig. 3). The solid gray lines separating quiescent and star-forming galaxies are derived from Schreiber et al. (2015). The dotted gray line separating quiescent galaxies into young-stellar-population- and old-stellar-population-dominated galaxies are derived from Whitaker et al. (2013).

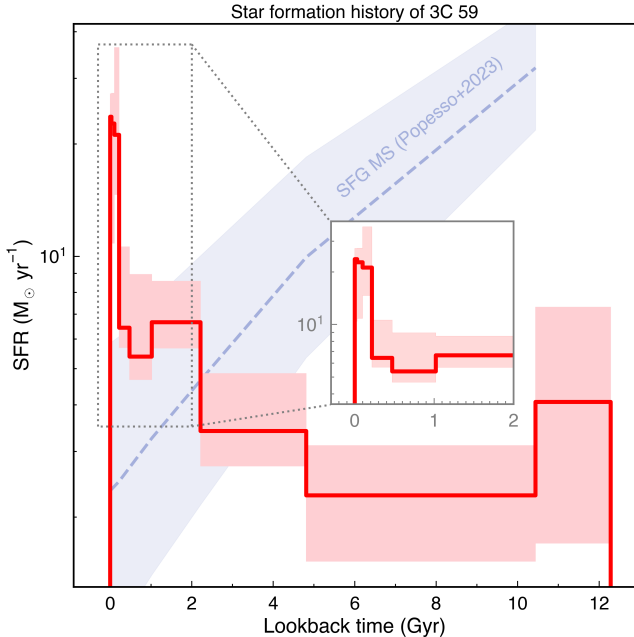


Figure 5. The star formation history of 3C 59. The red curve shows the best-fit star formation history of 3C 59 with PROSPECTOR, while the red region shows the $1\text{-}\sigma$ uncertainty. The small grey panel shows the star formation history after zooming in recent 2 Gyr. The dashed blue line represents the star-forming main sequence from Popesso et al. (2023), while the blue region represents the $1\text{-}\sigma$ uncertainty.

for recent star formation quenching, also excludes the possibility that they have already passed by 3C 59 and travel to larger distance with gas completely stripped. Therefore, gas stripping through galaxy interaction cannot fully explain the low star formation activities in all the satellite galaxies.

- (2) *Radio AGN feedback affect the satellites population.* Shabala et al. (2011) found that satellites lying in the projected path of the FR II radio jets are more prone to have star formation quenching than those outside the path, while the satellites in the path of FR I radio jets show similar star formation properties to those outside the path. 3C 59 shows FR II radio jets, but all satellite galaxies are offset from the radio lobes. It indicates that in this system, large-scale radio jets may not have a direct effect on the populations of these satellite galaxies, but an indirect way, such as heating the intergalactic medium to further reduce the star-formation in the satellites (e.g., Shen et al. 2019), still cannot be excluded.
- (3) *Massive dark matter halo prevents gas inflow.* Halo quenching is usually expected to operate in halo masses higher than $10^{12} M_{\odot}$, where halo gas

becomes shock-heated and gas supply to galaxies is further prevented (Birnboim & Dekel 2003; Dekel & Birnboim 2006). We adopted two methods to estimate the dark matter halo mass (M_h) of 3C 59: (i) $M_{\star}\text{-}M_h$ relation² in Girelli et al. (2020); (ii) $M_{\text{BH}}\text{-}M_h$ relation³ in Ferrarese (2002), where M_{BH} is the black hole mass. The M_{BH} of 3C 59 is estimated to be $10^{8.912} M_{\odot}$ through reverberation mapping method (Wu & Liu 2004). The method (i) obtained $M_{h,\star} = 9.48^{+2.76}_{-2.18} \times 10^{11} M_{\odot}$, while for method (ii), $M_{h,\text{BH}} = 1.44 \times 10^{13} M_{\odot}$. The $M_{h,\text{BH}}$ is 15 times larger than $M_{h,\star}$. According to the halo virial radius (R_{vir}) calculation⁴ from Dekel & Birnboim (2006), $M_{h,\star}$ and $M_{h,\text{BH}}$ correspond to $R_{\text{vir},\star} = 254^{+23}_{-21}$ kpc and $R_{\text{vir},\text{BH}} = 629$ kpc, respectively. According to Woo et al. (2015), for halo mass of $M_{h,\star}$, 10% to 60% satellites are quenched, while for halo mass of $M_{h,\text{BH}}$, 60% to 100% satellites are quenched. Assuming that the halo mass is approximate to $M_{h,\text{BH}}$ can fully explain the quiescent satellite fraction around 3C 59. Both of the above two methods show that the halo mass of 3C 59 is almost higher than $10^{12} M_{\odot}$, so halo quenching may have a significant impact on populations of satellite galaxies. In addition, ram-pressure stripping effect may also exist in this massive halo, which may also affect the gas supply and star formations in satellite galaxies.

Overall, these results indicate that the massive halo combined with the enormous power from the large-scale radio jet of 3C 59 may keep the halo hot, prevent gas cooling, and further reduce star formation in the satellite galaxies.

7. SUMMARY AND CONCLUSIONS

We witness a rare galaxy group system where the central radio-loud AGN 3C 59 is hosted by an elliptical galaxy with recent star formation rejuvenation and satellite galaxies are all quiescent disk galaxies. The main conclusions are as follows:

- (1) 3C 59 is a flat spectrum radio quasar with a large-scale radio jet extending to ~ 150 kpc. It is hosted by an elliptical galaxy (early-type galaxy) but undergoes a significant star formation rejuvenation within the past 500 Myr, before which remains rather quiescent for most of the cosmic time.

² $M_{\star}/M_h = 0.093 \times [(M_h/10^{11.77})^{-1.00} + (M_h/10^{11.77})^{0.702}]^{-1}$

³ $(M_{\text{BH}}/10^8 M_{\odot}) = 0.10 (M_h/10^{12} M_{\odot})^{1.65}$

⁴ $R_{\text{vir}} = 120 (M_h/10^{11} M_{\odot})^{1/3}$ kpc

- (2) 3C 59 has five satellite galaxies within a projected distance of 200 kpc. Three nearest satellite galaxies show significant morphological disturbances and two of them exhibit significant tidal tails pointing towards 3C 59. In addition, 3C 59 has larger effective radius than both of local late- and early-type galaxies. These pieces of evidences indicate a minor merger between 3C 59 and nearby satellite galaxies, which may further trigger the star formation rejuvenation in 3C 59. Minor mergers may be also responsible for triggering quasar activities.
- (3) All the satellite galaxies are disk galaxies (late-type galaxies), but do not have significant star formation activities. It may be due to the possibility that the massive halo combined with the enormous power from the large-scale radio jet of 3C 59 keep the halo hot, prevent gas cooling, and further reduce star formation in these satellite galaxies.

8. ACKNOWLEDGMENTS

We thank the anonymous referee for the constructive comments that improved this paper. We thank Fei Li, Lingrui Lin, Yulong Gao, Can Xu, Longyue Chen, Luwenjia Zhou, Min Bao, and Zhengyi Chen for helpful discussion in framing this work. This work was supported by National Natural Science Foundation of China (Project No. 12173017 and Key Project No. 12141301), National Key R&D Program of China (2023YFA1605600), and the China Manned Space Project (No. CMS-CSST-2021-A07). Y.J.W. acknowledges supports by National Natural Science Foundation of China (Project No. 12403019) and Jiangsu Natural Science Foundation (Project No. BK20241188). The DESI Legacy Imaging Surveys consist of three individual and complementary projects: the Dark Energy Camera Legacy Survey (DECaLS), the Beijing-Arizona Sky Survey (BASS), and the Mayall z-band Legacy Survey (MzLS). DECaLS, BASS and MzLS together include data obtained, respectively, at the Blanco telescope, Cerro Tololo Inter-American Observatory, NSF’s NOIRLab; the Bok telescope, Steward Observatory, University of Arizona; and the Mayall telescope, Kitt Peak National Observatory, NOIRLab. NOIRLab is operated by the Association of Universities for Research in Astronomy (AURA) under a cooperative agreement

with the National Science Foundation. Pipeline processing and analyses of the data were supported by NOIRLab and the Lawrence Berkeley National Laboratory (LBNL). Legacy Surveys also uses data products from the Near-Earth Object Wide-field Infrared Survey Explorer (NEOWISE), a project of the Jet Propulsion Laboratory/California Institute of Technology, funded by the National Aeronautics and Space Administration. Legacy Surveys was supported by: the Director, Office of Science, Office of High Energy Physics of the U.S. Department of Energy; the National Energy Research Scientific Computing Center, a DOE Office of Science User Facility; the U.S. National Science Foundation, Division of Astronomical Sciences; the National Astronomical Observatories of China, the Chinese Academy of Sciences and the Chinese National Natural Science Foundation. LBNL is managed by the Regents of the University of California under contract to the U.S. Department of Energy. The complete acknowledgments can be found at <https://www.legacysurvey.org/acknowledgment/>. Guoshoujing Telescope (the Large Sky Area Multi-Object Fiber Spectroscopic Telescope LAMOST) is a National Major Scientific Project built by the Chinese Academy of Sciences. Funding for the project has been provided by the National Development and Reform Commission. LAMOST is operated and managed by the National Astronomical Observatories, Chinese Academy of Sciences. This research has made use of the CIRADA cutout service at URL cutouts.cirada.ca, operated by the Canadian Initiative for Radio Astronomy Data Analysis (CIRADA). CIRADA is funded by a grant from the Canada Foundation for Innovation 2017 Innovation Fund (Project 35999), as well as by the Provinces of Ontario, British Columbia, Alberta, Manitoba and Quebec, in collaboration with the National Research Council of Canada, the US National Radio Astronomy Observatory and Australia’s Commonwealth Scientific and Industrial Research Organisation.

Facilities: GALEX (FUV and NUV), SDSS (u , g , r , i , and z), LAMOST, WISE (W1, W2, W3, and W4), IRAS, VLA (3 GHz), VLBI (4.3 GHz and 7.6 GHz)

Software: astropy (Astropy Collaboration et al. 2013, 2018), CIGALE (Burgarella et al. 2005; Noll et al. 2009; Boquien et al. 2019; Yang et al. 2020, 2022), GaLight (Ding et al. 2021)

APPENDIX

A. MULTI-WAVELENGTH PHOTOMETRIC DATA

The observational data at FUV and NUV filters of the Galaxy Evolution Explorer (GALEX) were derived from GALEX’s All-Sky Imaging Survey (Morrissey et al. 2007). The angular resolution is $4.2''$ for FUV filter and $5.3''$ for NUV filter (Morrissey et al. 2007). The $5\text{-}\sigma$ depth at FUV and NUV filters are $39.8\ \mu\text{Jy}$ and $17.4\ \mu\text{Jy}$, respectively (Morrissey et al. 2007; Bianchi et al. 2011).

The observed fluxes at u , g , r , i , and z bands of Sloan Digital Sky Survey (SDSS) were collected from the 16th data release of SDSS (Ahumada et al. 2020). A typical angular resolution of SDSS is about $1.2''$. The $5\text{-}\sigma$ depth at u , g , r , i , and z bands are $5.0\ \mu\text{Jy}$, $2.0\ \mu\text{Jy}$, $3.0\ \mu\text{Jy}$, $4.8\ \mu\text{Jy}$, and $18.8\ \mu\text{Jy}$, respectively⁵.

The Two Micron All-Sky Survey (2MASS) data in J ($1.25\ \mu\text{m}$), H ($1.65\ \mu\text{m}$), and Ks ($2.17\ \mu\text{m}$) filters were derived from Cutri et al. (2003). The angular resolutions for these three filters are about $4.0''$ ⁶. The $5\text{-}\sigma$ depth at J, H, and Ks filters are $0.39\ \text{mJy}$, $0.47\ \text{mJy}$, and $0.85\ \text{mJy}$, respectively (Cutri et al. 2003).

The Wide-field Infrared Survey Explorer (WISE) data in W1 ($3.4\ \mu\text{m}$), W2 ($4.6\ \mu\text{m}$), W3 ($12\ \mu\text{m}$), and W4 ($22\ \mu\text{m}$) bandpasses were collected from the ALLWISE program (Cutri et al. 2021). Angular resolution is $6.1''$ for W1, $6.4''$ for W2, $6.5''$ for W3, and $12.0''$ for W4 (Wright et al. 2010). The $5\text{-}\sigma$ depth in W1, W2, W3, and W4 bandpasses are $0.08\ \text{mJy}$, $0.11\ \text{mJy}$, $1.0\ \text{mJy}$, and $6.0\ \text{mJy}$, respectively (Wright et al. 2010).

The Infrared Astronomical Satellite (IRAS) mission observed 3C 59 at $12\ \mu\text{m}$, $25\ \mu\text{m}$, $60\ \mu\text{m}$, $100\ \mu\text{m}$ through IRAS Sky Survey Atlas (irs 2019), but did not find any counterpart. It might be due to the fact that the source fluxes are below the detection limits that is about $500\ \text{mJy}$ at $12\text{--}60\ \mu\text{m}$, and about $1500\ \text{mJy}$ at $100\ \mu\text{m}$ ⁷.

The lower limit of flux at $250\ \text{GHz}$ was obtained with the Max-Planck Millimeter Bolometer (MAMBO) at the IRAM 30m telescope, which was derived from van Bemmelen & Bertoldi (2001). The CIGALE cannot utilize lower limits of fluxes, so we only use this lower limit as a reference for whether the SED fitting at sub-millimeter is reliable.

The VLASS $3\ \text{GHz}$ photometric data was derived from Gordon et al. (2021). The angular resolution is about $2.5''$. The median rms for images is $128\ \mu\text{Jy beam}^{-1}$ (Gordon et al. 2021).

The $4.3\ \text{GHz}$ and $7.6\ \text{GHz}$ data detected by the very long baseline interferometry (VLBI) were derived from Petrov (2021). Both of these two bands have an angular resolution below $0.1''$. The characteristic image sensitivities⁸ at $4.3\ \text{GHz}$ and $7.6\ \text{GHz}$ are $\sim 5\ \text{mJy beam}^{-1}$ and $\sim 8\text{--}10\ \text{mJy beam}^{-1}$, respectively.

⁵ See details in https://www.sdss4.org/dr16/imaging/other_info/

⁶ See details in <https://www.ipac.caltech.edu/2mass/overview/about2mass.html>

⁷ See details in <https://lambda.gsfc.nasa.gov/product/iras/>

⁸ See details in <https://science.nrao.edu/facilities/vlba/docs/manuals/oss/bands-perf>

Table A1. Multi-wavelength data used for constructing the broadband SED of 3C 59.

Observatory/survey	Observation date	Reference	Filter/band	λ_{ref} (\AA) ¹	Flux (mJy) ²
GALEX	2007-9-10	Bianchi et al. (2011)	FUV	1535	0.210 ± 0.014
			NUV	2301	0.239 ± 0.010
SDSS	2009-10-17	Ahumada et al. (2020)	u	3557	0.670 ± 0.007
			g	4703	0.899 ± 0.003
			r	6176	1.376 ± 0.005
			i	7490	2.375 ± 0.009
			z	8947	2.299 ± 0.015
LAMOST ³	2016-01-12	LAMOST DR8	band-1	3973	0.644 ± 0.142
			band-2	5096	1.219 ± 0.110
			band-3	6126	1.297 ± 0.074
			band-4	6399	1.467 ± 0.068
			band-5	6763	1.557 ± 0.103
			band-6	7694	1.918 ± 0.114
			band-7	8197	2.114 ± 0.155
			band-8	8794	2.295 ± 0.220
2MASS	1999-11-24	Cutri et al. (2003)	J	12350	2.454 ± 0.108
			H	16620	3.265 ± 0.192
			K_s	21590	5.395 ± 0.194
WISE	2013	Cutri et al. (2021)	W1	33526	7.86 ± 0.17
			W2	46028	11.25 ± 0.23
			W3	115608	31.83 ± 0.50
			W4	220883	72.06 ± 1.92
IRAS ⁴	1983	irs (2019)	IRAS60	6×10^5	< 500
			IRAS100	10^6	< 1500
IRAM	1999 December	van Bemmell & Bertoldi (2001)	250 GHz	1.2×10^7	> 3
VLASS	2019-04-07	Gordon et al. (2021)	3 GHz	10^9	22.49 ± 0.80
VLBI ⁴	2015–2016	Petrov (2021)	4.3 GHz	7×10^8	15.0
			7.6 GHz	4×10^8	17.0

NOTE—¹ Reference wavelength of filters are provided by [Filter Profile Service](#) except for the LAMOST spectrum. ² The Galactic extinction corrections had been made for all the fluxes (see details in Section 3.2). ³ From the calibrated LAMOST spectrum, we select 8 continuum ranges (band-1 to band-8 here; see the yellow regions in Figure B1), and obtained the average wavelength and average flux of each range. ⁴ The flux uncertainties are not given by Petrov (2021), so we took 10% of fluxes as the flux uncertainties in the broadband SED fitting.

B. OPTICAL SPECTRUM OF 3C 59 FROM LAMOST

The one-dimensional (1D) LAMOST spectrum of 3C 59 was downloaded from the LAMOST DATA RELEASE 8 (DR8) low-resolution spectra website⁹. LAMOST spectra cover a wavelength range of 3700–9000 \AA with a spectral resolution of $R \sim 1000$ –2000. Each spectrum consists of a blue (3700–5900 \AA) and a red spectrograph arms (5700–9000 \AA)¹⁰. LAMOST only makes relative flux calibration rather than accurate absolute flux calibration, so we utilized SDSS multi-band (g , r , z) photometric data to recalibrate LAMOST red and blue spectra following Jin et al. (2023) (See Figure B1). We adopted the χ^2 minimum method to match the released LAMOST spectrum that only has the relative flux without units to the SDSS photometric data. Here we only used g , r , and z bands of SDSS data to make flux calibration without including u and i filters, because u band is out of the LAMOST spectrum coverage and i band

⁹ See the LAMOST DR8 website: <http://www.lamost.org/dr8/>

¹⁰ See the LAMOST website: <http://www.lamost.org/public/node/119?locale=en>

Table A2. Multi-wavelength data used for constructing the broadband SEDs of the five satellite galaxies (A, B, C, D, and E).

Observatory	Obs. date	Reference	Filter	λ_{ref} (\AA) ¹	Flux (mJy)				
					A	B	C	D	E
SDSS	2009-10-17	Ahumada et al. (2020)	u	3557	0.004 ± 0.003	0.005 ± 0.003	0.009 ± 0.005	0.014 ± 0.004	0.009 ± 0.002
			g	4703	0.034 ± 0.001	0.043 ± 0.001	0.094 ± 0.002	0.066 ± 0.001	0.035 ± 0.001
			r	6176	0.079 ± 0.002	0.089 ± 0.002	0.233 ± 0.003	0.161 ± 0.003	0.049 ± 0.001
			i	7490	0.108 ± 0.002	0.122 ± 0.003	0.350 ± 0.004	0.220 ± 0.003	0.064 ± 0.002
			z	8947	0.150 ± 0.010	0.152 ± 0.010	0.510 ± 0.016	0.295 ± 0.014	0.069 ± 0.007
2MASS	1999-11-24	Cutri et al. (2003)	H	16620	< 0.772
			K_s	21590	0.552 ± 0.069
WISE	2013	Cutri et al. (2021)	W1	33526	0.118 ± 0.006	0.154 ± 0.006	< 0.486	0.183 ± 0.007	0.062 ± 0.005
			W2	46028	0.055 ± 0.012	0.099 ± 0.011	< 0.327	0.130 ± 0.016	< 0.041

NOTE—¹ Reference wavelength of filters are provided by [Filter Profile Service](#). The projected distance between Satellite C and its projected neighbor galaxy is about $5.5''$, which is lower than the angular resolution of WISE ($> 6.0''$, see Appendix A). In [Cutri et al. \(2021\)](#), Satellite C and its neighbor belong to one WISE-detected source, so here we used the WISE fluxes as upper limits for Satellite C.

covers the wavelength range of $H\alpha$ emission lines (See Figure B1). During the re-calibration, we assumed that the spectral shape in the blue and red channels are not changed.

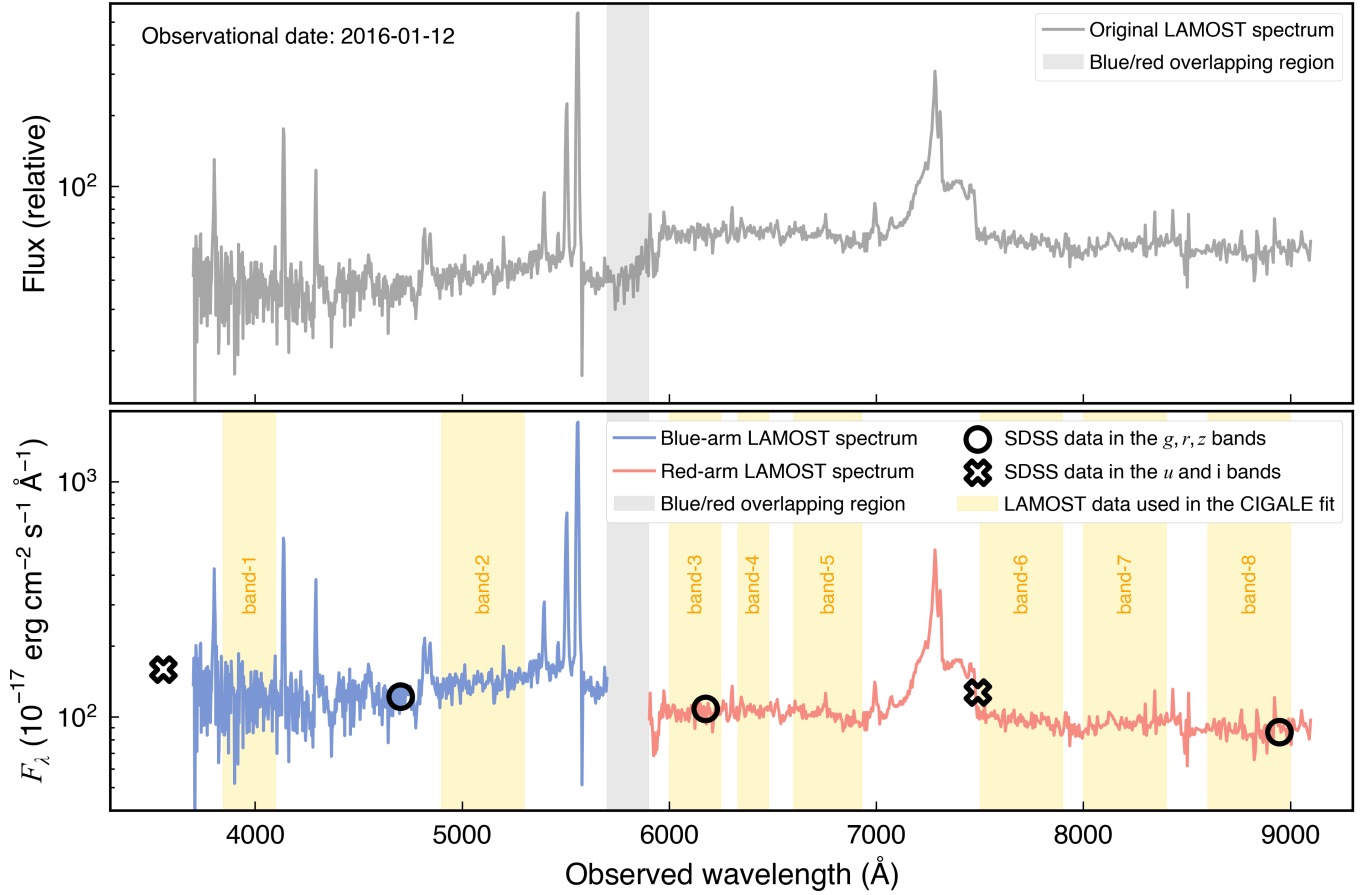


Figure B1. Absolute flux calibration for the LAMOST spectrum of 3C 59. *Top panel:* the original LAMOST spectrum only with the relative flux calibration. *Bottom panel:* the LAMOST spectrum after the absolute flux calibration. The blue and red curves represent the blue- and red-arm LAMOST spectra, respectively. The grey curve represents the overlapping region between the blue- and red-arm LAMOST spectrum (5700–5900 Å). The empty black circles represent the flux densities in the SDSS g , r , and z bands that are used in the flux calibration, while the empty black x-shape-symbols represent the flux densities in the SDSS u and i bands that are not used in the calibration (see details in Appendix B). The yellow regions represent the spectrum data that are used in the broadband SED fitting (see detailed values in Table A1).

C. 2D IMAGE DECOMPOSITION

Table C1. Best-fit structure properties for 3C 59 and the five satellite galaxies (A, B, C, D, and E) with GALIGHT

Parameter	Symbol	3C 59	A	B	C	D	E
<i>g</i> -filter							
Effective radius	$R_{e,g}$ (kpc)	8.86 ± 0.07	2.10 ± 0.05	2.79 ± 0.04	3.96 ± 0.05	4.01 ± 0.05	1.47 ± 0.03
Sérsic index	$n_{\text{sérsic},g}$	4.0*	1.61 ± 0.13	1.68 ± 0.07	1.26 ± 0.04	1.31 ± 0.04	0.78 ± 0.06
AGN fluxes	$S_{\text{AGN},g}$ (mJy)	0.16 ± 0.04
Reduced χ^2	χ_r^2	1.14	1.22	0.98	0.90	0.83	0.85
<i>r</i> -filter							
Effective radius	$R_{e,r}$ (kpc)	9.00 ± 0.06	1.66 ± 0.03	2.55 ± 0.04	3.47 ± 0.04	4.01 ± 0.05	1.00 ± 0.03
Sérsic index	$n_{\text{sérsic},r}$	4.0*	1.66 ± 0.16	1.96 ± 0.12	1.64 ± 0.05	1.31 ± 0.04	1.56 ± 0.24
AGN fluxes	$S_{\text{AGN},r}$ (mJy)	0.19 ± 0.01
Reduced χ^2	χ_r^2	1.12	1.58	1.05	0.95	0.83	0.76
<i>z</i> -filter							
Effective radius	$R_{e,z}$ (kpc)	8.85 ± 0.05	2.60 ± 0.21	3.08 ± 0.07	3.52 ± 0.04	4.02 ± 0.07	1.16 ± 0.05
Sérsic index	$n_{\text{sérsic},z}$	4.0*	$5.25^{+0.95}_{-0.76}$	2.18 ± 0.12	1.80 ± 0.04	2.18 ± 0.08	2.33 ± 0.36
AGN fluxes	$S_{\text{AGN},z}$ (mJy)	0.41 ± 0.03
Reduced χ^2	χ_r^2	1.08	1.26	1.07	1.01	0.85	0.78

NOTE—* The Sérsic index of 3C 59 is fixed to 4.0 during the image decomposition (see details in Section 4.1).

D. MODEL PARAMETERS FOR BROADBAND SED FITTING WITH CIGALE

Table D1. Model parameter settings in the SED fitting with only AGN and dust models for 3C 59

Module	Parameter	Symbol	Values
Galactic dust emission (Dale et al. 2014)	Slope in $dM_{\text{dust}} \propto U^{-\alpha} dU$	α	1.5 to 3.5 (step 0.125)
AGN (UV-to-IR) (Stalevski et al. 2012, 2016)	AGN contribution to IR luminosity	frac_{AGN}	0.05, 0.1 to 0.95 (step 0.05), 0.99
	Viewing angle *	θ	$0^\circ, 10^\circ, 20^\circ, 30^\circ, 40^\circ, 50^\circ$
	Polar-dust color excess	$E(B - V)_{\text{PD}}$ (mag)	0.1 to 1.5 (step 0.1)
Radio	SF radio-IR correlation parameter	q_{IR}	2.58^\dagger
	Radio-loudness parameter	R_{AGN}	2 to 50 (step 2)
	Spectral index of AGN radio emission	α_{AGN}	0.20 to 0.60 (step 0.01)

NOTE— † The star-formation radio-IR correlation parameter (q_{IR}) is fixed to the default value of CIGALE. * 3C 59 exhibits double-peaked broad emission lines (Eracleous & Halpern 1994; Mejía-Restrepo et al. 2022), which indicates a face-on orientation, so the viewing angle is set to be between 0° and 50° .

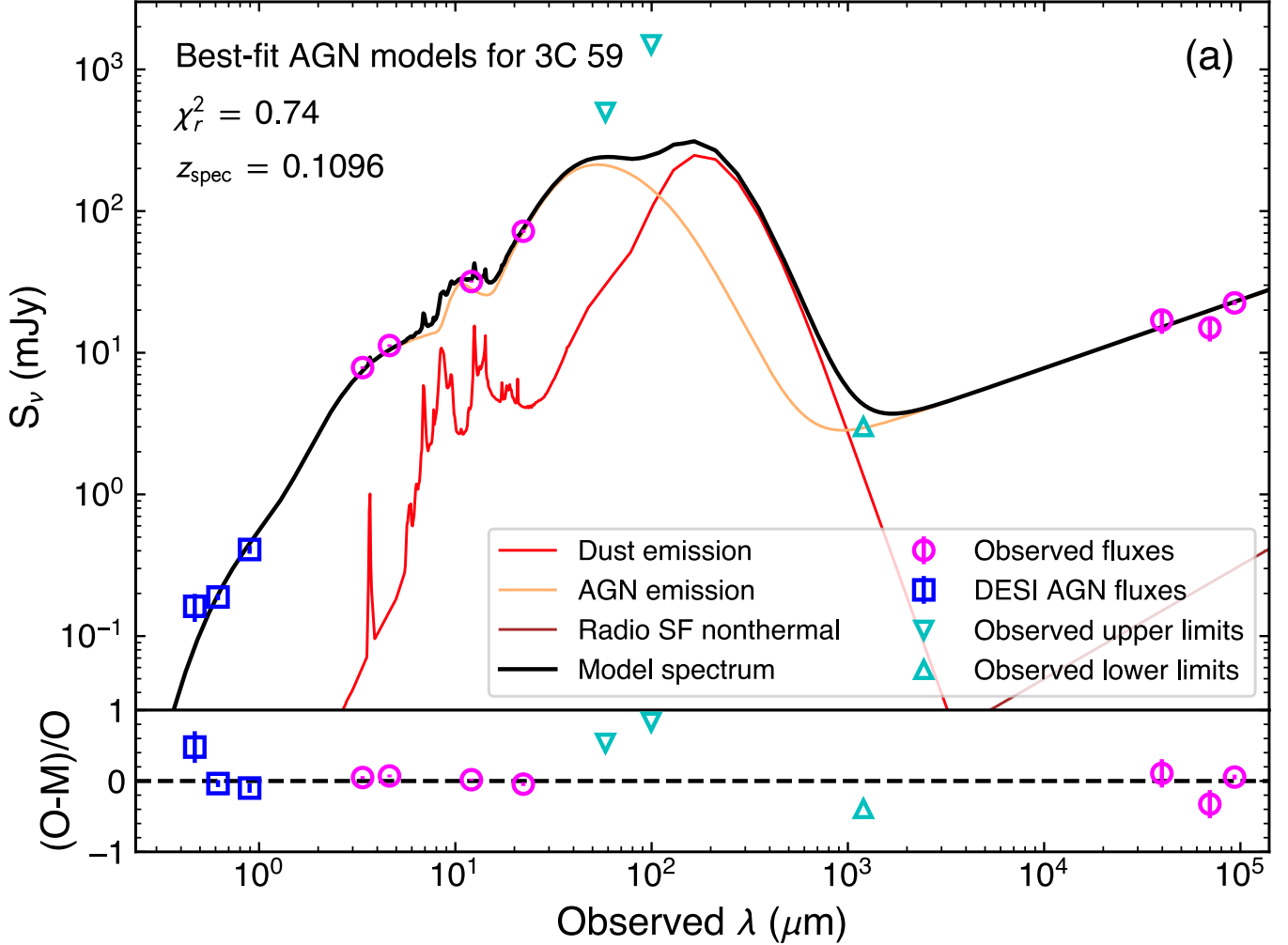


Figure D1. Best-fit SED model for AGN and dust components of 3C 59 with CIGALE. The observed fluxes and upper limits are shown in Table A1. The DESI AGN fluxes are listed in Table C1.

E. AGN PROPERTIES OF 3C 59

The physical properties of 3C 39 are summarize in Table 1. 3C 59 has a spectral index of AGN radio emission with $\alpha_{\text{AGN}} = -0.41 \pm 0.12$, which indicates that 3C 59 belongs to the flat spectrum radio quasars (FSRQs; $\alpha_{\text{AGN}} > -0.5$; Mao et al. 2017). Total 8–1000 μm infrared (IR) luminosity is around $(1.22 \pm 0.07) \times 10^{38}$ W, which is lower than the maximum IR luminosity with 2.16×10^{38} W predicted by the 3σ upper limit of IRAS 100 μm flux upper limit (Rothberg et al. 2013). The fraction of AGN IR luminosity to total IR luminosity (F_{AGN}) is $80\% \pm 11\%$, which indicates that the entire IR radiation of 3C 59 is dominated by the AGN emission. The radio loudness estimated through the SED fitting in this work is 14 ± 2 . The rest-frame 1.4 GHz radio luminosity ($L_{1.4\text{GHz,rest}}$) is 8.9×10^{23} W Hz^{-1} that is calculated by $L_{1.4\text{GHz,rest}} = 4\pi D_L^2 / (1+z)^{1+\alpha_{\text{AGN}}} \times (1.4/3)^{\alpha_{\text{AGN}}} \times S_{3\text{GHz,obs}}$ where $S_{3\text{GHz,obs}}$ is the observed integrated flux densities at VLA 3 GHz (Ceraj et al. 2018). Wang et al. (2024) obtained the probability of radio AGNs hosted by SFGs or QGs as a function of stellar mass, radio luminosity, and redshift. At the stellar mass, radio luminosity, and redshift of 3C 59, the corresponding probability of hosting radio AGNs in QGs is almost 2.5 times higher than that in SFGs, but 3C 59 is hosted by an SFG (see details in Section 6.1). Therefore, it is a special case.

Table D2. Model parameter settings in the entire SED fitting of 3C 59

Module	Parameter	Symbol	Values
Star formation history [SFR $\propto t \exp(-t/\tau)$]	Stellar e -folding time	τ_{star} (10^6 yr)	1, 10, 50, 70, 100 to 950 (step 50), 1000 to 3000 (step 100), 3500 to 10000 (step 500)
	Stellar age	t_{star} (10^6 yr)	50, 70, 100, 150, 170, 200, 220, 250, 300 to 1000 (step 50), 1000, 1600, 2500, 3600, 5000, 7000, 10000
Simple stellar population (Bruzual & Charlot 2003)	Initial mass function	–	Chabrier (2003)
	Metallicity	Z	0.0001, 0.0004, 0.004, 0.008, 0.02, 0.05
Dust attenuation (Calzetti et al. 2000)	Color excess of the nebular lines	$E(B - V)$ (mag)	0.005, 0.05, 0.1 to 0.5 (step 0.01), 0.55 to 1.5 (step 0.05)
Galactic dust emission (Dale et al. 2014)	Slope in $dM_{\text{dust}} \propto U^{-\alpha} dU$	α	3.5*
AGN (UV-to-IR) (Stalevski et al. 2012, 2016)	AGN contribution to IR luminosity	frac_{AGN}	0.8*
	Viewing angle	θ	30° *
	Polar-dust color excess	$E(B - V)_{\text{PD}}$ (mag)	0.8*
Radio	SF radio-IR correlation parameter	q_{IR}	2.58 [†]
	Radio-loudness parameter	R_{AGN}	14*
	Spectral index of AGN radio emission	α_{AGN}	0.48*

NOTE—[†] The q_{IR} is fixed to the default value of CIGALE. * These parameters are fixed to the best-fit values obtained in the SED fitting with only AGN and dust models (see details in Section 5.1).

Table D3. Model parameter settings in the SED fitting for the five satellite galaxies

Module	Parameter	Symbol	Values
Star formation history [SFR $\propto t \exp(-t/\tau)$]	Stellar e -folding time	τ_{star} (10^6 yr)	1, 10, 50, 70, 100 to 950 (step 50), 1000 to 3000 (step 100), 3500 to 10000 (step 500)
	Stellar age	t_{star} (10^6 yr)	50, 70, 100, 150, 170, 200, 220, 250, 300 to 1000 (step 50), 1000, 1600, 2500, 3600, 5000, 7000, 10000
Simple stellar population (Bruzual & Charlot 2003)	Initial mass function	–	Chabrier (2003)
	Metallicity	Z	0.0001, 0.0004, 0.004, 0.008, 0.02, 0.05
Dust attenuation (Calzetti et al. 2000)	Color excess of the nebular lines	$E(B - V)$ (mag)	0.005, 0.01, 0.025, 0.05, 0.075, 0.10 to 1.5 (step 0.05)

F. SED FITTING WITH PROSPECTOR FOR 3C 59

The modules, parameters, and prior functions used in the SED fitting with PROSPECTOR are shown in Table F1.

Table F1. Parameters and priors for SED fitting with PROSPECTOR for 3C 59

Module	Parameter	Description	Prior function [prior range]
Star formation history	$\log(M_*/M_\odot)$	Total stellar mass formed	Uniform [7, 12]
	$\log r_i$	Ratio of the SFRs between adjacent bins	StudentT(0, 0.3, 2)
	$\log(Z_*/Z_\odot)$	Stellar metallicity	Uniform [-2, 0.19]
Dust attenuation	dust1	Attenuation by dust of stellar birth clouds	Uniform [0.1, 5]
	dust2	Attenuation by dust of the diffuse interstellar medium	Uniform [0, 5]
	Γ_{dust}	Slope of Kriek & Conroy (2013) dust law	Uniform [-2, 0.5]
Nebular emission	$\log U_{\text{neb}}$	Ionization parameter of nebular emission	Uniform [-4, -1]
Dust emission	U_{min}	Minimum starlight intensity relative to the local interstellar radiation field	Uniform [0.1, 25]
	Q_{PAH}	Polycyclic aromatic hydrocarbon (PAH) mass fraction	Uniform [0.5, 7]
	γ_{dust}	Warm dust fraction	LogUniform [0.001, 0.15]

REFERENCES

2019, The IRAS Sky Survey Atlas, IPAC,

doi: [10.26131/IRSA10](https://doi.org/10.26131/IRSA10)

Ahumada, R., Allende Prieto, C., Almeida, A., et al. 2020,

ApJS, 249, 3, doi: [10.3847/1538-4365/ab929e](https://doi.org/10.3847/1538-4365/ab929e)

- Astropy Collaboration, Robitaille, T. P., Tollerud, E. J., et al. 2013, *A&A*, 558, A33, doi: [10.1051/0004-6361/201322068](https://doi.org/10.1051/0004-6361/201322068)
- Astropy Collaboration, Price-Whelan, A. M., Sipőcz, B. M., et al. 2018, *AJ*, 156, 123, doi: [10.3847/1538-3881/aabc4f](https://doi.org/10.3847/1538-3881/aabc4f)
- Beck, R., Dobos, L., Budavári, T., Szalay, A. S., & Csabai, I. 2016, *MNRAS*, 460, 1371, doi: [10.1093/mnras/stw1009](https://doi.org/10.1093/mnras/stw1009)
- Bédorf, J., & Portegies Zwart, S. 2013, *MNRAS*, 431, 767, doi: [10.1093/mnras/stt208](https://doi.org/10.1093/mnras/stt208)
- Bianchi, L., Herald, J., Efremova, B., et al. 2011, *Ap&SS*, 335, 161, doi: [10.1007/s10509-010-0581-x](https://doi.org/10.1007/s10509-010-0581-x)
- Birnboim, Y., & Dekel, A. 2003, *MNRAS*, 345, 349, doi: [10.1046/j.1365-8711.2003.06955.x](https://doi.org/10.1046/j.1365-8711.2003.06955.x)
- Boquien, M., Burgarella, D., Roehlly, Y., et al. 2019, *A&A*, 622, A103, doi: [10.1051/0004-6361/201834156](https://doi.org/10.1051/0004-6361/201834156)
- Bruzual, G., & Charlot, S. 2003, *MNRAS*, 344, 1000, doi: [10.1046/j.1365-8711.2003.06897.x](https://doi.org/10.1046/j.1365-8711.2003.06897.x)
- Burgarella, D., Buat, V., & Iglesias-Páramo, J. 2005, *MNRAS*, 360, 1413, doi: [10.1111/j.1365-2966.2005.09131.x](https://doi.org/10.1111/j.1365-2966.2005.09131.x)
- Calzetti, D., Armus, L., Bohlin, R. C., et al. 2000, *ApJ*, 533, 682, doi: [10.1086/308692](https://doi.org/10.1086/308692)
- Ceraj, L., Smolčić, V., Delvecchio, I., et al. 2018, *A&A*, 620, A192, doi: [10.1051/0004-6361/201833935](https://doi.org/10.1051/0004-6361/201833935)
- Chabrier, G. 2003, *ApJL*, 586, L133, doi: [10.1086/374879](https://doi.org/10.1086/374879)
- Chauke, P., van der Wel, A., Pacifici, C., et al. 2019, *ApJ*, 877, 48, doi: [10.3847/1538-4357/ab164d](https://doi.org/10.3847/1538-4357/ab164d)
- Cutri, R. M., Skrutskie, M. F., van Dyk, S., et al. 2003, *VizieR Online Data Catalog*, II/246
- Cutri, R. M., Wright, E. L., Conrow, T., et al. 2021, *VizieR Online Data Catalog*, II/328
- Dale, D. A., Helou, G., Magdis, G. E., et al. 2014, *ApJ*, 784, 83, doi: [10.1088/0004-637X/784/1/83](https://doi.org/10.1088/0004-637X/784/1/83)
- Dekel, A., & Birnboim, Y. 2006, *MNRAS*, 368, 2, doi: [10.1111/j.1365-2966.2006.10145.x](https://doi.org/10.1111/j.1365-2966.2006.10145.x)
- Dey, A., Schlegel, D. J., Lang, D., et al. 2019, *AJ*, 157, 168, doi: [10.3847/1538-3881/ab089d](https://doi.org/10.3847/1538-3881/ab089d)
- Diaz, J., Bekki, K., Forbes, D. A., et al. 2018, *MNRAS*, 477, 2030, doi: [10.1093/mnras/sty743](https://doi.org/10.1093/mnras/sty743)
- Ding, X., Birrer, S., Treu, T., & Silverman, J. D. 2021, *arXiv e-prints*, arXiv:2111.08721, doi: [10.48550/arXiv.2111.08721](https://doi.org/10.48550/arXiv.2111.08721)
- Eracleous, M., & Halpern, J. P. 1994, *ApJS*, 90, 1, doi: [10.1086/191856](https://doi.org/10.1086/191856)
- . 2004, *ApJS*, 150, 181, doi: [10.1086/379823](https://doi.org/10.1086/379823)
- Faber, S. M., Willmer, C. N. A., Wolf, C., et al. 2007, *ApJ*, 665, 265, doi: [10.1086/519294](https://doi.org/10.1086/519294)
- Ferrarese, L. 2002, *ApJ*, 578, 90, doi: [10.1086/342308](https://doi.org/10.1086/342308)
- Fitzpatrick, E. L. 1999, *PASP*, 111, 63, doi: [10.1086/316293](https://doi.org/10.1086/316293)
- Girelli, G., Pozzetti, L., Bolzonella, M., et al. 2020, *A&A*, 634, A135, doi: [10.1051/0004-6361/201936329](https://doi.org/10.1051/0004-6361/201936329)
- Gordon, Y. A., Boyce, M. M., O’Dea, C. P., et al. 2021, *ApJS*, 255, 30, doi: [10.3847/1538-4365/ac05c0](https://doi.org/10.3847/1538-4365/ac05c0)
- Hao, C.-N., Shi, Y., Chen, Y., et al. 2019, *ApJL*, 883, L36, doi: [10.3847/2041-8213/ab42e5](https://doi.org/10.3847/2041-8213/ab42e5)
- Jin, J.-J., Wu, X.-B., Fu, Y., et al. 2023, *ApJS*, 265, 25, doi: [10.3847/1538-4365/acaf89](https://doi.org/10.3847/1538-4365/acaf89)
- Johnson, B. D., Leja, J., Conroy, C., & Speagle, J. S. 2021, *ApJS*, 254, 22, doi: [10.3847/1538-4365/abef67](https://doi.org/10.3847/1538-4365/abef67)
- Kaviraj, S., Peirani, S., Khochfar, S., Silk, J., & Kay, S. 2009, *MNRAS*, 394, 1713, doi: [10.1111/j.1365-2966.2009.14403.x](https://doi.org/10.1111/j.1365-2966.2009.14403.x)
- Kaviraj, S., Huertas-Company, M., Cohen, S., et al. 2014, *MNRAS*, 443, 1861, doi: [10.1093/mnras/stu1220](https://doi.org/10.1093/mnras/stu1220)
- Kriek, M., & Conroy, C. 2013, *ApJL*, 775, L16, doi: [10.1088/2041-8205/775/1/L16](https://doi.org/10.1088/2041-8205/775/1/L16)
- Kroupa, P. 2001, *MNRAS*, 322, 231, doi: [10.1046/j.1365-8711.2001.04022.x](https://doi.org/10.1046/j.1365-8711.2001.04022.x)
- Lacy, M., Baum, S. A., Chandler, C. J., et al. 2020, *PASP*, 132, 035001, doi: [10.1088/1538-3873/ab63eb](https://doi.org/10.1088/1538-3873/ab63eb)
- Lange, R., Driver, S. P., Robotham, A. S. G., et al. 2015, *MNRAS*, 447, 2603, doi: [10.1093/mnras/stu2467](https://doi.org/10.1093/mnras/stu2467)
- Leja, J., Johnson, B. D., Conroy, C., van Dokkum, P. G., & Byler, N. 2017, *ApJ*, 837, 170, doi: [10.3847/1538-4357/aa5ffe](https://doi.org/10.3847/1538-4357/aa5ffe)
- López-Sanjuán, C., Le Fèvre, O., Ilbert, O., et al. 2012, *A&A*, 548, A7, doi: [10.1051/0004-6361/201219085](https://doi.org/10.1051/0004-6361/201219085)
- Mancini, C., Daddi, E., Juneau, S., et al. 2019, *MNRAS*, 489, 1265, doi: [10.1093/mnras/stz2130](https://doi.org/10.1093/mnras/stz2130)
- Mao, P., Urry, C. M., Marchesini, E., et al. 2017, *ApJ*, 842, 87, doi: [10.3847/1538-4357/aa74b8](https://doi.org/10.3847/1538-4357/aa74b8)
- Matharu, J., Muzzin, A., Brammer, G. B., et al. 2019, *MNRAS*, 484, 595, doi: [10.1093/mnras/sty3465](https://doi.org/10.1093/mnras/sty3465)
- Mejía-Restrepo, J. E., Trakhtenbrot, B., Koss, M. J., et al. 2022, *ApJS*, 261, 5, doi: [10.3847/1538-4365/ac6602](https://doi.org/10.3847/1538-4365/ac6602)
- Morrissey, P., Conrow, T., Barlow, T. A., et al. 2007, *ApJS*, 173, 682, doi: [10.1086/520512](https://doi.org/10.1086/520512)
- Moustakas, J., Coil, A. L., Aird, J., et al. 2013, *ApJ*, 767, 50, doi: [10.1088/0004-637X/767/1/50](https://doi.org/10.1088/0004-637X/767/1/50)
- Naab, T., Johansson, P. H., & Ostriker, J. P. 2009, *ApJL*, 699, L178, doi: [10.1088/0004-637X/699/2/L178](https://doi.org/10.1088/0004-637X/699/2/L178)
- Noeske, K. G., Weiner, B. J., Faber, S. M., et al. 2007, *ApJL*, 660, L43, doi: [10.1086/517926](https://doi.org/10.1086/517926)
- Noll, S., Burgarella, D., Giovannoli, E., et al. 2009, *A&A*, 507, 1793, doi: [10.1051/0004-6361/200912497](https://doi.org/10.1051/0004-6361/200912497)
- Oogi, T., Habe, A., & Ishiyama, T. 2016, *MNRAS*, 456, 300, doi: [10.1093/mnras/stv2581](https://doi.org/10.1093/mnras/stv2581)
- Pandey, D., Kaviraj, S., Saha, K., & Sharma, S. 2024, *MNRAS*, 531, 2223, doi: [10.1093/mnras/stae1296](https://doi.org/10.1093/mnras/stae1296)

- Paudel, S., Yoon, S.-J., Bait, O., et al. 2023, *ApJL*, 951, L36, doi: [10.3847/2041-8213/acdef1](https://doi.org/10.3847/2041-8213/acdef1)
- Peng, Y.-j., Lilly, S. J., Kovač, K., et al. 2010, *ApJ*, 721, 193, doi: [10.1088/0004-637X/721/1/193](https://doi.org/10.1088/0004-637X/721/1/193)
- Petrov, L. 2021, *AJ*, 161, 14, doi: [10.3847/1538-3881/abc4e1](https://doi.org/10.3847/1538-3881/abc4e1)
- Popesso, P., Concas, A., Cresci, G., et al. 2023, *MNRAS*, 519, 1526, doi: [10.1093/mnras/stac3214](https://doi.org/10.1093/mnras/stac3214)
- Rathore, H., Kumar, K., Mishra, P. K., Wadadekar, Y., & Bait, O. 2022, *MNRAS*, 513, 389, doi: [10.1093/mnras/stac871](https://doi.org/10.1093/mnras/stac871)
- Renzini, A., & Peng, Y.-j. 2015, *ApJL*, 801, L29, doi: [10.1088/2041-8205/801/2/L29](https://doi.org/10.1088/2041-8205/801/2/L29)
- Rothberg, B., Fischer, J., Rodrigues, M., & Sanders, D. B. 2013, *ApJ*, 767, 72, doi: [10.1088/0004-637X/767/1/72](https://doi.org/10.1088/0004-637X/767/1/72)
- Rowlands, K., Wild, V., Bourne, N., et al. 2018, *MNRAS*, 473, 1168, doi: [10.1093/mnras/stx1903](https://doi.org/10.1093/mnras/stx1903)
- Schlafly, E. F., & Finkbeiner, D. P. 2011, *ApJ*, 737, 103, doi: [10.1088/0004-637X/737/2/103](https://doi.org/10.1088/0004-637X/737/2/103)
- Schlegel, D. J., Finkbeiner, D. P., & Davis, M. 1998, *ApJ*, 500, 525, doi: [10.1086/305772](https://doi.org/10.1086/305772)
- Schreiber, C., Pannella, M., Elbaz, D., et al. 2015, *A&A*, 575, A74, doi: [10.1051/0004-6361/201425017](https://doi.org/10.1051/0004-6361/201425017)
- Shabala, S. S., Kaviraj, S., & Silk, J. 2011, *MNRAS*, 413, 2815, doi: [10.1111/j.1365-2966.2011.18353.x](https://doi.org/10.1111/j.1365-2966.2011.18353.x)
- Shen, L., Tomczak, A. R., Lemaux, B. C., et al. 2019, *MNRAS*, 484, 2433, doi: [10.1093/mnras/stz152](https://doi.org/10.1093/mnras/stz152)
- Speagle, J. S., Steinhardt, C. L., Capak, P. L., & Silverman, J. D. 2014, *ApJS*, 214, 15, doi: [10.1088/0067-0049/214/2/15](https://doi.org/10.1088/0067-0049/214/2/15)
- Stalevski, M., Fritz, J., Baes, M., Nakos, T., & Popović, L. Č. 2012, *MNRAS*, 420, 2756, doi: [10.1111/j.1365-2966.2011.19775.x](https://doi.org/10.1111/j.1365-2966.2011.19775.x)
- Stalevski, M., Ricci, C., Ueda, Y., et al. 2016, *MNRAS*, 458, 2288, doi: [10.1093/mnras/stw444](https://doi.org/10.1093/mnras/stw444)
- Tacchella, S., Conroy, C., Faber, S. M., et al. 2022, *ApJ*, 926, 134, doi: [10.3847/1538-4357/ac449b](https://doi.org/10.3847/1538-4357/ac449b)
- Tanaka, T. S., Shimasaku, K., Tacchella, S., et al. 2024, *PASJ*, 76, 1, doi: [10.1093/pasj/psad076](https://doi.org/10.1093/pasj/psad076)
- van Bemmell, I. M., & Bertoldi, F. 2001, *A&A*, 368, 414, doi: [10.1051/0004-6361:20010040](https://doi.org/10.1051/0004-6361:20010040)
- Wang, T., Xu, K., Wu, Y., et al. 2023, arXiv e-prints, arXiv:2311.07653, doi: [10.48550/arXiv.2311.07653](https://doi.org/10.48550/arXiv.2311.07653)
- Wang, Y., Wang, T., Liu, D., et al. 2024, *A&A*, 685, A79, doi: [10.1051/0004-6361/202347787](https://doi.org/10.1051/0004-6361/202347787)
- Whitaker, K. E., van Dokkum, P. G., Brammer, G., et al. 2013, *ApJL*, 770, L39, doi: [10.1088/2041-8205/770/2/L39](https://doi.org/10.1088/2041-8205/770/2/L39)
- Woo, J., Dekel, A., Faber, S. M., & Koo, D. C. 2015, *MNRAS*, 448, 237, doi: [10.1093/mnras/stu2755](https://doi.org/10.1093/mnras/stu2755)
- Wright, E. L., Eisenhardt, P. R. M., Mainzer, A. K., et al. 2010, *AJ*, 140, 1868, doi: [10.1088/0004-6256/140/6/1868](https://doi.org/10.1088/0004-6256/140/6/1868)
- Wu, X.-B., & Liu, F. K. 2004, *ApJ*, 614, 91, doi: [10.1086/423446](https://doi.org/10.1086/423446)
- Yang, G., Boquien, M., Buat, V., et al. 2020, *MNRAS*, 491, 740, doi: [10.1093/mnras/stz3001](https://doi.org/10.1093/mnras/stz3001)
- Yang, G., Boquien, M., Brandt, W. N., et al. 2022, *ApJ*, 927, 192, doi: [10.3847/1538-4357/ac4971](https://doi.org/10.3847/1538-4357/ac4971)